frontiers | Frontiers in Physics

TYPE Original Research
PUBLISHED 27 November 2024
DOI 10.3389/fphy.2024.1426469

OPEN ACCESS

EDITED BY
Jianglei Di,
Guangdong University of Technology, China

REVIEWED BY
Irina Nakashidze,
Shota Rustaveli State University, Georgia
Jinlong Zhu,
Huazhong University of Science and Technology, China

*CORRESPONDENCE
Yurii Ushenko,
yuriyu@gmail.com

RECEIVED 01 May 2024
ACCEPTED 30 October 2024
PUBLISHED 27 November 2024

CITATION
Ushenko O, Bilookyi O, Zheng J, Dubolazov A, Olar O, Ushenko Y, Soltys I, Mikirin I, Skliarchuk V and Chen Z (2024) 3D digital holographic polarimetry of laser speckle fields formed by polycrystalline blood films: a tool for differential diagnosis of thyroid pathology. *Front. Phys.* 12:1426469. doi: 10.3389/fphy.2024.1426469

3D digital holographic polarimetry of laser speckle fields formed by polycrystalline blood films: a tool for differential diagnosis of thyroid pathology

Olexander Ushenko[1,2], Olexander Bilookyi[3], Jun Zheng[1], Alexander Dubolazov[2], Olexander Olar[2,4], Yurii Ushenko[4,5]*, Iryna Soltys[2], Ivan Mikirin[2], Valeriy Skliarchuk[2] and Zhebo Chen[1]

[1]Taizhou Institute of Zhejiang University, Taizhou, China, [2]Optics and Publishing Department, Chernivtsi National University, Chernivtsi, Ukraine, [3]Department of Surgery No 1, Bucovinian State Medical University, Chernivtsi, Ukraine, [4]Computer Science Department, Chernivtsi National University, Chernivtsi, Ukraine, [5]Department of Physics, Shaoxing University, Shaoxing, Zhejiang, China

The principles and effectiveness of the method of laser polarization interferometry of dehydrated blood films (facies) for the differential diagnosis of thyroid pathology have been studied. For this purpose, a theoretical description of the processes of formation and layer-by-layer phase scanning of the polarization structure of speckle fields in the blood facies of donors and patients with nodular goiter, autoimmune thyroiditis, and papillary cancer has been developed for the first time. A statistical analysis of holographically reconstructed maps of polarization ellipticity of the singly scattered component of the speckle field was conducted. Based on this analysis, the most sensitive markers for the diagnosis and differentiation of thyroid pathology were identified. Excellent diagnostic accuracy (91%–93%) and very good differentiation accuracy (86%–89%) were achieved for nodular goiter, autoimmune thyroiditis, and papillary cancer.

KEYWORDS

polarization, interference, holography, microscopic image, optical anisotropy, statistical moments, blood facies, thyroid gland

1 Introduction

Non-destructive remote photometric, spectral, correlation and polarization optical methods have been widely used to study the optically inhomogeneous structure of biological objects [1–5].

Polarization studies turned out to be one of the most diagnostically promising methods for detecting the optical manifestations of the polycrystalline architecture of biological tissues and fluids [6]. Studies have demonstrated the potential of polarimetry for diagnosing cataracts in the lens, monitoring glucose concentration in the tissues of diabetic patients, and detecting malignant changes [7–12].

The successful diagnostic development of polarimetry of biological layers contributed to the formation of new Mueller matrix techniques, leading to the establishment of Mueller matrix microscopy (MMM) as a separate branch [13–19]. The methodological basis of MMM is various theoretical models and methods of analysis. The most effective were regression models of optical anisotropy [14] and logarithmic Mueller matrix decomposition [15–18]. The MMM results are objectively assessed within the statistical analysis framework of Mueller matrix images and optical anisotropy maps [14, 18]. This provided the possibility of obtaining quantitative optical metrics to characterize the evolution of gastric tissue from a healthy state through inflammation to cancer using Mueller microscopy of gastric biopsies [14].

Further development of the functionality of MMM methods ensured the use of a broader class of analytical algorithms - correlation, fractal, wavelet, Fourier, and singular analysis - for quantitative data processing [20–29].

One of these methods' promising applications may be diagnosing thyroid gland pathological conditions.

Timely thyroid pathology detection is one of the global health problems. According to statistics from the World Health Organization, 10%–30% of the adult population worldwide suffers from various diseases associated with the thyroid gland, which are associated with both gland dysfunction and changes in its structure. Moreover, this figure increases by 5% every year [30].

Traditionally, the gold standard for diagnosing thyroid pathology is biopsy or surgical resection of tissue sections stained with hematoxylin and eosin visual microscopic evaluation. However, early diagnosis is difficult due to the variability of the tissue morphological interpretation. In addition, cancerous change areas may be small and hardly noticeable.

These methods have become the digital pathology direction, using new quantitative image analysis possibilities. In [31], thin sections of the thyroid nodules capsule, microscopic images, histograms, and texture analysis were used. On this basis, the possibility of a differential diagnosis for the thyroid nodules as benign (follicular adenoma) or malignant (papillary carcinoma) was demonstrated.

Thus, pathologists can improve thyroid pathology diagnosis by applying new objective quantitative technologies with high spatial resolution [32].

Among such technologies, polarization-sensitive second harmonic generation (PSHG) microscopy methods can be distinguished [33, 34].

PSHG microscopy techniques are used to differentiate cancerous or diseased tissues by analyzing circular dichroism and modulating laser polarization states.

As a result, it is possible to measure ultrastructural changes in the collagen frameworks of organ tissues in submicron areas.

This microscopic technique has been used to study the collagen organization in both benign and malignant fibrillar capsules of the thyroid.

The possibility of differentiating follicular adenoma and papillary carcinoma node capsules has been demonstrated [35]. The obtained quantitative information about the collagen capsule can significantly complement traditional histopathological examination.

The development and addition of PSHG microscopy are methods of non-invasive polarization-sensitive optical coherence tomography (PSOCT) [36–44].

The use of the principles of direct interference recording of the structure of object speckle fields provided the possibility of layer-by-layer measurement of the coordinate distributions of elements of the Mueller matrix or Mueller matrix images (MMI) at various depths of biological objects. In this case, the possibility of quantitative layer-by-layer assessment of the optical anisotropy of biological tissue is realized [36, 45]. As a result, it was possible to diagnose fibrosis and differentiate tumor sites with low fibrosis accurately. However, the sensitivity of such systems was limited by t a high level of depolarized laser speckle background.

Biological tissue object fields phase scanning polarization-interference methods with complex amplitude distributions layer-by-layer digital reconstruction can eliminate the influence of such background and increase PSHG and PSOCT techniques' diagnostic sensitivity [45–52].

These methods allow the phase separation of a singly scattered (non-depolarized) component in a laser speckle field. The biological layer complex amplitude field non-depolarized component uniquely relates to the optically anisotropic component parameters. As a result, it becomes possible to obtain, within the statistical analysis framework, the most accurate information about pathological changes in the human tissue biopsy samples polycrystalline architectonics diagnosed. On this basis, the possibility of diagnosing endometriosis [48], differentiating benign and malignant prostate tumors [45, 49] and necrotic and traumatic changes in the myocardium [52] have been demonstrated.

An expansion of the functionality of the polarization-interference phase scanning methods can be the study of different kinds of objects, such as biological fluids. Such objects are easily accessible and do not require traumatic biopsy surgery. These objects are one of the most essential systems for ensuring the body's vital activity, which is a set of biological fluids involved in metabolic processes. In biological fluids (BF), there are high-speed changes in the molecular composition and the interaction of various components of physiological nature, as well as extreme and pathological conditions.

Any physiological or pathological process occurring in a living organism represents specific changes in the structure of protein and other organic molecules. Such changes are the most informative in the study of homeostasis at the molecular level and can serve as a basis for various diseases at the earliest stages of diagnosis [53, 54].

Modern laboratory and clinical diagnostics focus mainly on the numerous quantitative indicators contained in BF determination, which are products of body vital activity.

Morphological research in biology and medicine focuses mainly on cellular elements, while BF morphological analysis - the life support basic system–has remained inaccessible for clinical practice until recently [55]. A BF drop lying on a horizontal plane is a self-organizing system that is a convenient model for studying physical-chemical processes. Its properties are determined by the dissolved substances in a liquid composition, external dehydration conditions, and the substrate material. As a BF drop dehydration result, a dry film is formed–a "facia", the structure of which carries information about the composition and relationships of substances dissolved in BF. By studying such objects at the self-organization macroscopic

level, the researcher receives information about the system at the molecular level behaviour [56–59].

One of the most informative biological fluids about the state of the human body is blood, which contains about 100 different proteins. Conventionally (according to differences in solubility), they are divided into five main fractions: albumins (55%–65%), α1 - (2%–4%), α2 - (6%–12%), β - (8%–12%) and γ – (2%–4%) globulins.

The albumin concentration in the blood is high, and its molecule size is small. Therefore, the albumin molecules collection total surface area is extensive. As a result, they are well suited to perform the transport function - bilirubin, urobilin, fatty acids, bile salts, and lipid hormones. The albumin fraction also includes transthyretin (prealbumin), which, together with thyroxine-binding globulin [*TBG*] and albumin, transports the thyroid hormone thyroxine and its metabolite iodothyronine.

Globulins are a blood proteins family, in the molecules of which polypeptide chains are tightly coiled into compact spherical structures - globules (tertiary protein structures). One globulin type is thyroglobulin (*Tg*). This is a protein produced by the thyroid gland follicular cells, accumulating in its structural and functional unit - the follicle - as a colloid. Patients with Hashimoto's thyroiditis or Graves' disease often have antithyroglobulin antibodies elevated levels. This indicator is used for diagnostic purposes. *Tg* is a differentiated (papillary or follicular) thyroid cancer reliable prognostic postoperative marker. In addition, *Tg* levels may be elevated in Graves' disease [60–68].

Such objects' optically anisotropic structure polarization characteristics have not been studied sufficiently. Only a few publications focus on using polarization interferometry of biological fluids to diagnose pathological changes in human organs [69].

Our work is focused on finding new objective markers for minimally invasive differential diagnosis of thyroid pathology using comprehensive polarization-interference mapping and digital holographic reconstruction of layer-by-layer maps of the ellipticity of speckle fields in blood facies. To achieve maximum effectiveness of the method, statistical analysis of the polarization ellipticity maps of the singly scattered component of the speckle field of the blood facies of donors and patients with nodular goiter, autoimmune thyroiditis, and papillary cancer has been applied for the first time.

2 A brief theoretical remarks

2.1 Optical anisotropy of blood facies

The Mueller matrix formalism is the theoretical basis for blood facies object fields laser polarimetry [11–19]. This approach provides the most complete description of the blood facies' optically anisotropic structure polarization manifestations [21, 69].

Based on the biological layer model developed in numerous studies [20–29], the following expressions for the circular and linear birefringence Mueller matrices can be derived for blood facies.

The matrix operator $\{\Omega\}$, which describes the optical activity at each individual point (r), has the following form

$$\{\Omega\}(r) = \begin{Vmatrix} 1 & 0 & 0 & 0 \\ 0 & \omega_{22} & \omega_{23} & 0 \\ 0 & \omega_{32} & \omega_{33} & 0 \\ 0 & 0 & 0 & 1 \end{Vmatrix}(r) \tag{1}$$

where

$$\omega_{ik}(r) = \begin{cases} \omega_{22} = \omega_{33} = cos\,2\vartheta, \\ \omega_{23} = -\omega_{32} = sin\,2\vartheta. \end{cases} \tag{2}$$

Here (r) – geometric coordinate in the biological layer plane (x,y); ϑ is the polarization plane rotation angle.

Linear birefringence optical manifestations of supramolecular networks at each point (r) are characterized by the Mueller matrix $\{D\}$

$$\{D\}(r) = \begin{Vmatrix} 1 & 0 & 0 & 0 \\ 0 & d_{22} & d_{23} & d_{24} \\ 0 & d_{32} & d_{33} & d_{34} \\ 0 & d_{42} & d_{43} & d_{44} \end{Vmatrix}(r) \tag{3}$$

where

$$d_{ik}(r) = \begin{cases} d_{22} = cos^2 2\rho + sin^2 2\rho\, cos\,\delta, \\ d_{23} = d_{32} = cos\,2\rho\, sin\,2\rho(1 - cos\,\delta), \\ d_{33} = sin^2 2\rho + cos^2 2\rho\, cos\,\delta, \\ d_{42} = -d_{24} = sin\,2\rho\, sin\,\delta, \\ d_{34} = -d_{43} = cos\,2\rho\, sin\,\delta, \\ d_{44} = cos\,\delta. \end{cases} \tag{4}$$

Here ρ - the optical axis direction; $\delta_{xy} = \frac{2\pi}{\lambda}\Delta n l$ - phase shift between the laser amplitude orthogonally polarized components E_x, E_y; λ - wavelength; Δn - birefringence value; l is the blood facie geometric thickness.

The resulting matrix operator is determined, which characterizes the integral manifestations of the blood facies' circular and linear birefringence.

$$\{F\}(r) = (\{\Omega\}(r))(\{D\}(r)) = \begin{Vmatrix} 1 & 0 & 0 & 0 \\ 0 & (d_{22}\omega_{22} + d_{32}\omega_{23}) & (d_{23}\omega_{22} + d_{33}\omega_{23}) & (d_{24}\omega_{22} + d_{34}\omega_{23}) \\ 0 & (d_{22}\omega_{32} + d_{32}\omega_{33}) & (d_{23}\omega_{32} + d_{33}\omega_{33}) & (d_{24}\omega_{32} + d_{34}\omega_{33}) \\ 0 & d_{42} & d_{43} & d_{44} \end{Vmatrix}(r) \tag{5}$$

2.2 Blood facies polarization maps

When the blood facies are irradiated with a polarized beam, local azimuth $\alpha(r)$ and ellipticity $\beta(r)$ values are formed.

The polarization parameters values are calculated from the following matrix equation

$$S_{pas}(x,y) = \{F(x,y)\}S_{in} \tag{6}$$

Here S_{in} i S_{pas} – irradiating and object optical fields Stokes vectors.

In the expanded form, Equation 6 is written as follows

$$\begin{pmatrix} S_1 \\ S_2 \\ S_3 \\ S_4 \end{pmatrix}_{pas}(x,y) = \begin{Vmatrix} 1 & 0 & 0 & 0 \\ 0 & f_{22} & f_{23} & f_{24} \\ 0 & f_{32} & f_{33} & f_{34} \\ 0 & f_{42} & f_{43} & f_{44} \end{Vmatrix}(x,y) \begin{pmatrix} S_1 \\ S_2 \\ S_3 \\ S_4 \end{pmatrix}_{in} \quad (7)$$

In the general case, the following relationship is realized between the azimuth $\alpha(x,y)$ and the ellipticity $\beta(x,y)$ coordinate distributions and the Stokes vector $S_{pas}(x,y)$ parameters values

$$\begin{pmatrix} S_1 \\ S_2 \\ S_3 \\ S_4 \end{pmatrix}_{pas}(x,y) = \begin{pmatrix} 1 \\ \cos 2\alpha \cos 2\beta \\ \sin 2\alpha \cos 2\beta \\ \sin 2\beta \end{pmatrix}(x,y) \quad (8)$$

The following expressions for the azimuth and ellipticity polarization maps are obtained from Equation 8

$$\alpha(x,y) = \left\{0.5\, arctan\left[\frac{S_3^{pas}}{S_2^{pas}}\right]\right\}(x,y) \quad (9)$$

$$\beta(x,y) = \left\{0.5\, arcsin\left[\frac{S_4^{pas}}{S_1^{pas}}\right]\right\}(x,y) \quad (10)$$

The most common case for serial polarization studies is the azimuthal-invariant mapping [21–30] implementation by using a circularly polarized irradiating beam $S_{in} = \begin{pmatrix} 1 \\ 0 \\ 0 \\ 1 \end{pmatrix}$.

Under such conditions, taking into account Equations 1–10 can be rewritten as follows

$$S_{pas}(x,y) = \begin{pmatrix} 1 \\ (d_{24}\omega_{22} + d_{34}\omega_{23}) \\ (d_{24}\omega_{32} + d_{34}\omega_{33}) \\ d_{44} \end{pmatrix}(x,y) \quad (11)$$

$$\alpha(x,y) = \left\{0.5\, arctan\left(\frac{d_{24}\omega_{32} + d_{34}\omega_{33}}{d_{24}\omega_{22} + d_{34}\omega_{23}}\right)\right\}(x,y) \quad (12)$$

$$\alpha(x,y) = \left\{0.5\, arctan\left[\frac{\sin 2(\rho - \vartheta)}{\sin 2(\rho + \vartheta)}\right]\right\}(x,y) \quad (13)$$

$$\beta(x,y) = \{0.5\, arcsin(d_{44})\}(x,y) \quad (14)$$

$$\beta(x,y) = \left\{0.5\, arcsin\left(\cos\delta_{xy}\right)\right\}(x,y) \quad (15)$$

Therefore, the conducted theoretical consideration of the optically anisotropic blood facies object field polarization structure formation revealed analytical relationships between:

- optically active (ϑ) protein molecules orientational structure (ρ) and polarization azimuth maps $\alpha(x,y)$ (Equation 13);
- supramolecular networks phase-shifting properties (δ) and polarization ellipticity maps $\beta(x,y)$ (Equation 15).

Laser object fields complex amplitudes $E(x,y)$ are phase-stationary distributions [39–43]. Taking into account this fact, we will use the known analytical relationship between the Stokes vector parameters (relation (8)) and the complex amplitude orthogonal components $\left(E_x, E_y\right)$ at each point of the field with the coordinate $r \equiv x,y$

$$S_1(r) = \left(E_x^* E_x + E_y^* E_y\right)(r) \quad (16)$$

$$S_2(r) = \left(E_x^* E_x - E_y^* E_y\right)(r) \quad (17)$$

$$S_3(r) = \left(E_x^* E_y + E_y^* E_x\right)(r) \quad (18)$$

$$S_4(r) = i\left[\left(E_y^* E_x - E_x^* E_y\right)\right](r) \quad (19)$$

Here "*" – denotes complex conjugation.

Taking into account Equations 16–19 for the polarization-interference determination of the blood facies speckle field azimuth $\alpha(x,y)$ and ellipticity $\beta(x,y)$ distributions, the following algorithm was used

$$\alpha(x,y) = \left\{0.5\, arctan\left[\frac{\left(E_x^* E_y + E_y^* E_x\right)}{\left(E_x^* E_x - E_y^* E_y\right)}\right]\right\} \quad (20)$$

$$\beta(x,y) = \left\{0.5\, arcsin\left[\frac{i\left[E_y^* E_x - E_x^* E_y\right]}{E_x^* E_x + E_y^* E_y}\right]\right\} \quad (21)$$

Taking into account Equations 20, 21, the analytical equation of polarization states at the points of the blood facies single scattered ("object") laser field component can be written in the following form

$$\frac{X^2}{E_x^2(r)} + \frac{Y^2}{E_y^2(r)} - \frac{2XY}{E_x(r)E_y(r)}\cos\delta_{xy}(r) = \sin^2\delta_{xy}(r) \quad (22)$$

Relations Equation 22 and Equations 12–19 determine the polarization structure of the single scattered component $E_{object}(r)$ of the object field of blood facies

$$E_{object}(r) \equiv \begin{pmatrix} E_x; \\ E_y; \\ \delta_{xy}; \\ \alpha(\rho \pm \theta); \\ \beta\left(\delta_{xy}\right) \end{pmatrix}(r) \quad (23)$$

This component $E_{object}(r)$ is uniquely related to the orientation $(\rho \pm \theta)$ and phase (δ_{xy}) of blood facies of optically anisotropic supramolecular networks parameters (13, 15). In this sense, the $E_{object}(r)$ distributions are diagnostically relevant and most sensitive to the blood facies polycrystalline architectonics with various transformations of thyroid pathologies. However, formed elements form coherent laser radiation with multiple scattering in the blood facies volume. This results in the different waves interference addition and the polarization-inhomogeneous speckle field U_{spekle} formation. This process can be analytically described as follows.

For the orthogonal components E_{xj} and E_{yj} of the complex amplitudes E_1 and E_2 of two partials singly scattered coherent waves

at a local point (r) in the blood facie object field, the following interference equations can be written:

$$\tilde{E}_{xj}(r) = \left(\tilde{E}_{x1} + \tilde{E}_{x2}\right)_j(r) = \left(\left|\tilde{E}_{x1}\right| + \left|\tilde{E}_{x2}\right| + 2\sqrt{\left|\tilde{E}_{x1}\right|\left|\tilde{E}_{x2}\right|}\cos\varphi_{x12}\right)_j(r) \tag{24}$$

$$\tilde{E}_{yj}(r) = \left(\tilde{E}_{y1} + \tilde{E}_{y2}\right)_j(r) = \left(\left|\tilde{E}_{y1}\right| + \left|\tilde{E}_{y2}\right| + 2\sqrt{\left|\tilde{E}_{y1}\right|\left|\tilde{E}_{y2}\right|}\cos\varphi_{y12}\right)_j(r) \tag{25}$$

where $\left|\tilde{E}_{xj}\right|(r); \left|\tilde{E}_{yj}\right|(r)$ – modules of complex amplitudes; $\varphi_{x12}(r)$ and $\varphi_{y12}(r)$ – phase shifts between $\left(\tilde{E}_{x1}; \tilde{E}_{x2}\right)(r)$ and $\left(\tilde{E}_{y1}; \tilde{E}_{y2}\right)(r)$.

For the process of forming the resulting orthogonal components of amplitudes U_x and U_y due to the "n-fold" interaction of the laser probe with optical heterogeneities, the following equations can be written:

$$U_x = \sum_{j=1}^{n}\tilde{E}_{xj};\ U_y = \sum_{j=1}^{n}\tilde{E}_{yj};\ \varphi_{xy} = \sum_{i=1}^{n}\varphi_{xj} - \sum_{i=1}^{n}\varphi_{yj} \tag{26}$$

In this way, a coordinate-distributed (x, y) interference (speckle) polarization-inhomogeneous component $U_{spekle}\left(U_x, U_y, \varphi_{xy}, \tilde{\alpha}, \tilde{\beta}\right)$ in the blood facies object field is formed with the following azimuth and polarization ellipticity values

$$\tilde{\alpha}(x,y) = \left\{0.5\,arctan\left[\frac{\left(\sum_{j=1}^{n}\tilde{E}^{*}_{xj}\sum_{j=1}^{n}\tilde{E}_{yj} + \sum_{j=1}^{n}\tilde{E}^{*}_{yj}\sum_{j=1}^{n}\tilde{E}_{xj}\right)}{\left(\sum_{j=1}^{n}\tilde{E}^{*}_{xj}\sum_{j=1}^{n}\tilde{E}_{xj} - \sum_{j=1}^{n}\tilde{E}^{*}_{yj}\sum_{j=1}^{n}\tilde{E}_{yj}\right)}\right]\right\} \tag{27}$$

$$\tilde{\beta}(x,y) = \left\{0.5\,arcsin\left[\frac{i\left[\sum_{j=1}^{n}\tilde{E}^{*}_{yj}\sum_{j=1}^{n}\tilde{E}_{xj} - \sum_{j=1}^{n}\tilde{E}^{*}_{xj}\sum_{j=1}^{n}\tilde{E}_{yj}\right]}{\sum_{j=1}^{n}\tilde{E}^{*}_{xj}\sum_{j=1}^{n}\tilde{E}_{xj} + \sum_{j=1}^{n}\tilde{E}^{*}_{yj}\sum_{j=1}^{n}\tilde{E}_{yj}}\right]\right\} \tag{28}$$

In this case, the analytical equation of polarization (Equation 22) at the points x, y of the multiply scattered speckle field, taking into account Equation 26, takes the following form

$$\frac{X^2}{\left|\sum_{j=1}^{n}\tilde{E}_{xj}\right|^2_x} + \frac{Y^2}{\left|\sum_{j=1}^{n}\tilde{E}_{yj}\right|^2_y} - \frac{2XY}{\left|\sum_{j=1}^{n}\tilde{E}_{xj}\right|\left|\sum_{j=1}^{n}\tilde{E}_{yj}\right|}\cos\left(\sum_{i=1}^{n}\varphi_{xj} - \sum_{i=1}^{n}\varphi_{yj}\right) = sin^2\left(\sum_{i=1}^{n}\varphi_{xj} - \sum_{i=1}^{n}\varphi_{yj}\right) \tag{29}$$

According to Equations 27–29, the polarization structure of the speckle field component $U_{spekle}(x,y)$ of blood facies is determined by the specificity of the complex amplitudes coordinate distribution U_x, U_y and the phase shifts φ_{xy} between them

$$U_{spekle}(x,y) \equiv \begin{pmatrix} U_x; \\ U_y; \\ \varphi_{xy}; \\ \tilde{\alpha}\left(\varphi_{xy}\right); \\ \tilde{\beta}\left(\varphi_{xy}\right) \end{pmatrix}(x,y) \tag{30}$$

For such a component $U_{spekle}(x,y)$ there is no unambiguous connection with the orientation $(\rho \pm \theta)$ and phase (δ_{xy}) parameters of the blood facies supramolecular networks (Equations 13, 15). In this sense, the distributions of $U_{spekle}(x,y)$ turn out to be integrally averaged and less sensitive to blood facies polycrystalline architectonics pathological transformations.

Thus, the polarization structure of real laser field $H_{blood\,facie}(x,y)$ scattered by blood facies can be represented as the following components superposition

$$H_{blood\,facie}(x,y) = E_{object}(x,y) + U_{spekle}(x,y) \tag{31}$$

$$\begin{pmatrix} H_x; \\ H_y; \\ \vartheta_{xy}; \\ \alpha\left(\vartheta_{xy}\right); \\ \beta_{blood\,facie}\left(\vartheta_{xy}\right) \end{pmatrix} = \begin{pmatrix} E_x; \\ E_y; \\ \delta_{xy}; \\ \alpha(\rho \pm \theta); \\ \beta_{object}\left(\delta_{xy}\right) \end{pmatrix}(x,y) + \begin{pmatrix} U_x; \\ U_y; \\ \varphi_{xy}; \\ \tilde{\alpha}\left(\varphi_{xy}\right); \\ \tilde{\beta}_{speckle}\left(\varphi_{xy}\right) \end{pmatrix}(x,y) \tag{32}$$

From Equations 31, 32 it follows that the thyroid pathology diagnostics efficiency is determined by the ratio between $E_{object}(x,y)$ and $U_{spekle}(x,y)$. "Minimization" of the influence of the $U_{spekle}(x,y)$ component turns out to be relevant for increasing sensitivity. It is impossible to implement such a procedure by the Stokes polarimetric mapping traditional method (6–15). In this case, phase information (δ_{xy} and φ_{xy}) is lost and only the intensity distributions $I_x = \left(\left|H_x\right|\right)^2$ and $I_y = \left(\left|H_y\right|\right)^2$ are measured. Therefore, we used another experimental technique–polarization interferometry, which provides the possibility of the complex amplitudes $H_{blood\,facie}(x,y) = E_{object}(x,y) + U_{spekle}(x,y)$ field algorithmic reconstruction with subsequent discrete scanning $\Delta\vartheta_{xy}$ of the phase set ϑ_{xy}. The scanning final result (Equation 33) is the selection of a single scattered component complex amplitudes distribution

$$\Delta\vartheta_{xy} \rightarrow \delta_{xy} \rightarrow \begin{pmatrix} E_x; \\ E_y; \\ \delta_{xy}; \\ \alpha(\rho \pm \theta); \\ \beta_{object}\left(\delta_{xy}\right) \end{pmatrix} \tag{33}$$

3 Optical scheme and brief theory of the method

In Figure 1 shows the polarization Mach-Zehnder interferometer scheme.

Publications present the characteristics of the polarization interferometry scheme [45–52]. Our work will analyse the laser field polarimetry method by reconstructing the complex amplitude distributions $H_{spekle}(x,y)$ to detect a single scattering component $E_{object}(x,y)$. For this purpose, we present the device's structural and logical diagram and analyze the main digital algorithms.

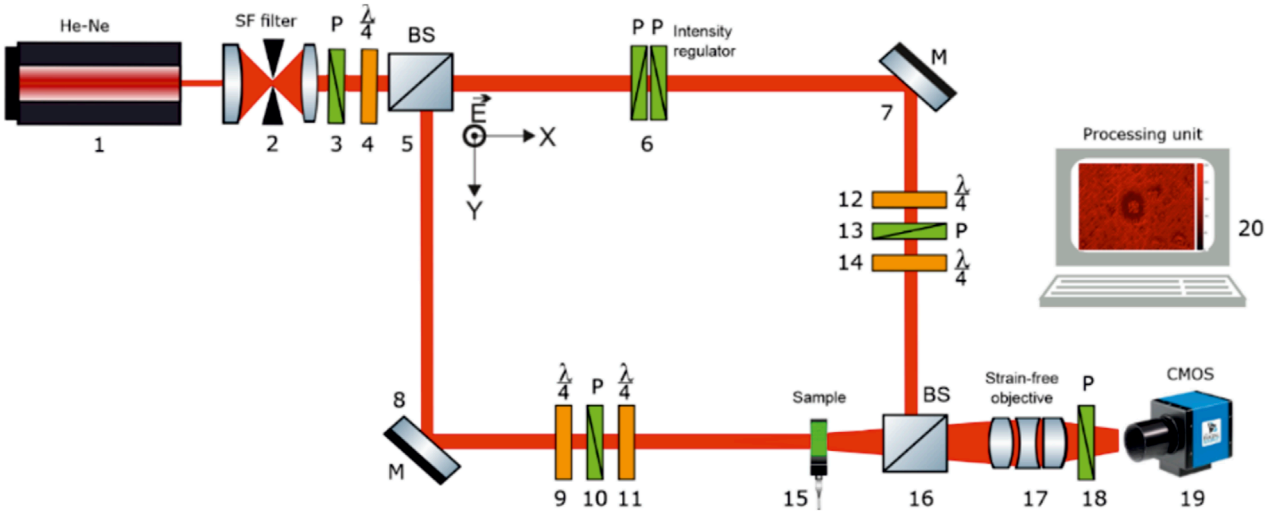

FIGURE 1
Optical polarization-interference scheme.

The polarization interferometer includes the following main blocks:

A. Polarizing illuminator, which generates a circularly polarized laser wave:

- He-Ne ($\lambda = 0.6328\mu m$) laser 1;
- collimator 2;
- polarizing filter (polarizer three and quarter-wave plate 4, the angle between the polarizer three transmission axes and the plate 4 highest speed axis is 45^0).

B. Reference channel:

- beam splitter 5;
- polarization intensity attenuator 6;
- rotating mirror 7;
- universal polarization filter (quarter-wave plates 12, 14 and polarizer 13) can form arbitrary polarization states.

C. Object channel:

- beam splitter 5;
- rotating mirror 8;
- universal polarization filter (quarter-wave plates 9, 11 and polarizer 10), which generates arbitrary polarization states;
- biological tissue sample 15.

D. Polarization filtering channel of the object field interference distribution:

- optical mixer 16;
- polarizing microlens 17;
- polarizer-analyzer 18 with an orientation of the transmission plane at angles $\Omega = 0^0$; $\Omega = 90^0$.

E. Digital recording and computer analysis unit

- digital camera 19;
- PC 20.

Parallel ($\varnothing = 2 \times 10^3 \mu m$) He-Ne ($\lambda = 0.6328\mu m$) laser 1 beam, formed by spatial-frequency filter 2, with 50% beam splitter three is divided into "object" and "reference" ones.

The "object" beam with the rotating mirror 5 help is directed through the polarizing filter 6–7 (manufacturer - Achromatic True Zero-Order Waveplate and manufacturer - B+ W Kaesemann XS-Pro Polarizer MRC Nano) in the blood facie 8 sample direction. The blood facie polarization-inhomogeneous image is projected by the strain-free objective 12 (manufacturer - Nikon CFI Achromat P, focal length - 30 mm, numerical aperture - 0.1, magnification - 4x) into the digital camera 14 (The Imaging Source DMK 41AU02. AS, monochrome 1/2"CCD, Sony ICX205AL (progressive scan) resolution - 1280 × 960, size of the photosensitive area - 7600 × 6200 μm; sensitivity - 0.05 lx; dynamic range - 8 bit, SNR - 9 bit), the photosensitive area, which contains $m \times n = 1280 \times 960$ pixels) plane.

The "reference" beam is directed by mirror 4 through the polarization filter 9–10 (manufacturer: Achromatic True Zero-Order Waveplate and manufacturer: B+ W Kaesemann XS-Pro Polarizer MRC Nano) into the blood facie polarization image plane.

As a result, an interference pattern is formed, the coordinate intensity distribution of which is recorded by a digital camera 14 through a polarizer 13.

Before carrying out blood facies measurements, the experimental device passed metrological certification with the model objects introduction ("clean air", "linear polarizer", "phase plates 0.25λ", "0.5λ"). As 50 measurements result for each type of object, the polarization ellipticity errors were determined $\beta = 0.0003 rad$.

The specified interferometer is modified for the experimental implementation of the blood facies fields of ellipticity β polarimetry (21, 28).

For each position of the polarizer-analyzer 18 transmission plane ($I_{\Omega=0^0;90^0}(m,n)$) in order to reconstruct the complex amplitudes ($H_{x;\Omega=0^0}(m,n)$; $H_{y;\Omega=90^0}(m,n)$), the two-dimensional digital Fourier transform algorithm $DFT(\upsilon,\nu)$ [45–52]

$$DFT_{\Omega=0^0;90^0}(\upsilon,\nu)=\frac{1}{M\times N}\sum_{m=0}^{M-1}\sum_{n=0}^{N-1}I_{\Omega=0^0;90^0}(m,n)\,exp\left[-i2\pi\left(\frac{m\times\upsilon}{M}+\frac{n\times\nu}{N}\right)\right] \quad (34)$$

where $I_{\Omega=0^0;90^0}(m,n)=H_{\Omega=0^0;90^0}(m,n)H^{*}_{\Omega=0^0;90^0}(m,n)$ are the intensity of interference pattern filtered by the analyzer with the transmission axis at $\Omega=0^0$; $\Omega=90^0$ orientation; $H_{\Omega=0^0;90^0}(m,n)$ are the complex amplitudes orthogonal projections; (υ,ν) are the spatial frequencies in the m and n directions respectively; (M,N) are the CCD camera pixels number – $0\le m,\upsilon\le M$ and $0\le n,\nu\le N$.

4. The digital Fourier transform results (Equation 34) for a circularly polarized (⊗) illuminating laser beam are used to obtain complex amplitude distributions according to the following algorithms

$$H_{0^0}\rightarrow\left|H_x^{\otimes}(\Omega=0^0)\right| \quad (35)$$

$$H_{90^0}\rightarrow\left|H_y^{\otimes}(\Omega=90^0)\right|exp\left(i\left(\theta_y^{\otimes}-\theta_x^{\otimes}\right)\right) \quad (36)$$

$$\theta_{xy}=\theta_y^{\otimes}-\theta_x^{\otimes} \quad (37)$$

Here θ_{xy} – phase differences between complex amplitude $H^{\otimes}$ orthogonal components $H_x^{\otimes}$, $H_y^{\otimes}$.

5. By reconstructing complex amplitudes field (35–37), phase scanning means $\theta_{xy}\Longrightarrow\theta_k\Longrightarrow\begin{pmatrix}E_x;\\E_y;\\\beta(\delta_{xy})\end{pmatrix}$ that we can obtain (21) the single scattering component polarization maps $\beta(\theta_k,m,n)$.
6. The quantitative criterion for determining the polarization map $\beta(\theta_k,m,n)$ is based on the algorithm for calculating the 1st to 4th orders central statistical moments in each phase section $\Delta\theta_{xy}$

$$\begin{aligned}SM_1&=\frac{1}{K}\sum_{j=1}^{K}\beta\left(\Delta\theta_{xy}\right)_j;\\SM_2&=\sqrt{\frac{1}{K}\sum_{j=1}^{K}\left(\beta\left(\Delta\theta_{xy}\right)^2\right)_j};\\SM_3&=\frac{1}{SM_2^3}\frac{1}{K}\sum_{j=1}^{K}\left(\beta\left(\Delta\theta_{xy}\right)^3\right)_j;\\SM_4&=\frac{1}{SM_2^4}\frac{1}{K}\sum_{j=1}^{K}\left(\beta\left(\Delta\theta_{xy}\right)^4\right)_j,\end{aligned} \quad (38)$$

where K – CCD pixels quantity.

7. By means of step-by-step phase comparison of the values $SM_{g=1;2;3;4}\left(\beta\left(\Delta\theta_{xy}\right)\right)$, the value θ_k was determined, starting from which the polarization maps $\beta\left(\Delta\theta_{xy},m,n\right)$ statistical structure turns out to be unchanged - $SM_{g=1;2;3;4}\left(\beta\left(\Delta\theta_{xy}\le\theta_k\right)\right)\approx const$.

4 Biological samples

4.1 Clinical and laboratory criteria for the formation of patient groups

Four representative dehydration blood facies groups were formed:

4.1.1 Control group

Healthy donors aged 30–60 years 51, patients (48 women, three men).

Inclusion criteria. Puncture biopsy of the thyroid gland without confirmed pathological processes. The normal level of thyroid hormones and autoantibodies.

Exclusion criteria. A puncture biopsy of the thyroid gland with pathological processes is confirmed in this organ.

4.1.2 Experimental group

51 patients aged 30–60 (46 women, 5 men) for nodular goiter.

Inclusion criteria. Puncture biopsy of the thyroid gland with pathological process confirmation. One or several thyroid gland colloid nodes are present. The normal level of thyroid hormones and autoantibodies.

Exclusion criteria. Increased or decreased level of thyroid hormones, increased level of autoantibodies. Associated pathology: diabetes, hypertension, atherosclerosis, chronic adrenal insufficiency, rheumatoid arthritis, chronic active hepatitis, systemic lupus erythematosus.

A violation of the principle of negative feedback endocrine function regulation characterizes this group.

4.1.3 Experimental group

51 patients aged 30–60 (49 women, 2 men) with autoimmune thyroiditis.

Inclusion criteria. Puncture biopsy of the thyroid gland with confirmation of the pathological process of stage 1–3 (1 - hypertrophic thyroiditis (Hashimoto's goiter), 2 - atrophic thyroiditis, 3 - fibrous invasive Riedel's goiter). Increased level of autoantibodies over 1000 IU/mL. Hypothyroidism.

Exclusion criteria. Increased level of thyroid hormones and autoantibodies to thyroperoxidase normal level. Associated pathology: diabetes, hypertension, atherosclerosis, chronic adrenal insufficiency, rheumatoid arthritis, chronic active hepatitis, systemic lupus erythematosus. Damage to the hematothyroid barrier is characteristic of this group.

4.1.4 Experimental group

51 patients aged 30–60 (44 women, 7 men) with papillary cancer thyroid gland.

Inclusion criteria. Puncture biopsy of the thyroid gland with pathological process confirmation - the papillary epithelium cancerous cells presence. Absence of germination outside the

TABLE 1 The blood films optical parameters.

Parameter	Group 1	Group 2	Group 3	Group 4
Attenuation coefficient τ, cm^{-1}	0.64 ± 0.04	0.61 ± 0.04	0.63 ± 0.04	0.62 ± 0.04
Depolarization degree $\Lambda, \%$	41± 0.9	38 ± 0.8	42 ± 0.8	40 ± 0.7

capsule and invasion of lymph nodes. The level of autoantibodies is normal. Euthyroidism.

Exclusion criteria. Increased or decreased thyroid hormone levels, increased autoantibodies to thyroperoxidase. Associated pathology: diabetes, hypertension, atherosclerosis, chronic adrenal insufficiency, rheumatoid arthritis, chronic active hepatitis, systemic lupus erythematosus. This group is characterized by uncontrolled, atypical growth of thyroid cells with the formation of papillary structures, the presence of nuclear inclusions, tumor progression, and a history of frequent exposure to the consequences of the Chernobyl accident.

Table 1 presents the polycrystalline blood films optical parameters.

The polycrystalline blood films extinction coefficient (τ, cm^{-1}) was measured according to the standard intensity attenuation photometry method [70] using an integral light scattering [71].

Depolarization degree measurement was performed in the standard Mueller matrix polarimeter scheme [20–29].

5 Experimental results and their discussion

At present, the tendencies of pathological transformation of polarization maps of optically anisotropic components of thyroid biopsy have been experimentally studied [72–75]:

- nodular goiter–growth of optical activity (1, 2) of thyroglobulin protein complexes due to enlargement of follicles and formation of structural birefringence (3, 4) as a result of the nodular proliferation of connective tissue;
- autoimmune thyroiditis–due to squamous cell metaplasia of follicular cells, an increase in their size forms proportionate manifestations of optical activity of thyroglobulin complexes and birefringence of the fibrous cord network;
- papillary cancer–predominant influence of structural birefringence due to hyperplasia in the form of elongated papillary formations.

Analysis and diagnostic use of the obtained results are based on a two-component amorphous anisotropic model of the optical properties of the thyroid gland. According to this model, the amorphous component (parenchyma formed by epithelial tissue) is polarization-inactive and does not change the polarization state of laser radiation. The anisotropic component consists of optically active (globulin protein complexes - follicles filled with a colloid of thyroglobulin proteins) and structural (supramolecular fibrillar protein networks of connective tissue in the parenchyma) components (5). The optically active component predominantly forms maps of polarization azimuth $\alpha(m,n)$, - relations (9, 12, 13). The structural or polycrystalline component predominantly forms maps of polarization ellipticity, - relations (10, 14, 15).

During the blood drop dehydration process, the natural self-assembly of protein molecules forms a supramolecular protein network. The structural characteristics of these proteins determine the formation of blood facies. The arrangement of atoms within the protein molecules defines their structure, which, in three-dimensional space, forms polymers or polypeptides. A sequence forms each polypeptide monomer or different α-amino acid. All α-amino acids found in living organisms, except glycine, contain an asymmetric carbon atom (threonine and isoleucine contain two asymmetric atoms) and have optical activity or circular birefringence [58, 69].

The protein structure hierarchy following levels are distinguished [64–68].

The primary structure of monomers (nucleotides or amino acids) represents the sequence. An amino acid's primary structure's significant feature is the almost random arrangement of its residues. From the biophysics perspective, circular birefringence is formed at this level.

The main polypeptide protein chain conformational arrangement forms the secondary structure, regardless of the side chains' conformation. At this level, the linear birefringence optical axis direction is formed.

The tertiary structure represents the protein molecule spatial structure, which consists of a single chain. According to the polypeptide chain in space spatial arrangement method, globular and fibrillar proteins are divided. Globular proteins most often have an ellipsoidal shape and predominantly exhibit circular birefringence. Fibrillar (thread-like) proteins have an elongated shape and exhibit linear birefringence.

The quaternary structure is formed by the spatial arrangement of the individual polypeptide chains, which have predominantly the same primary, secondary, and tertiary structure.

As a result, a structurally and functionally unified blood facies supramolecular network is formed, which has phase anisotropy - circular and linear birefringence. The specificity of blood facies proteins' polycrystalline supramolecular network structure or the relationship between the optical anisotropy parameter values is polypeptide fragments manifested in a certain conformational autonomy that are included in its composition.

Based on this, we should expect changes in the blood facies supramolecular networks' circular and linear birefringence parameters, depending on the presence of thyroid pathology. In our case, the following prognostic scenario is expected. A pathological increase in the thyroglobulin and the albumins concentration that

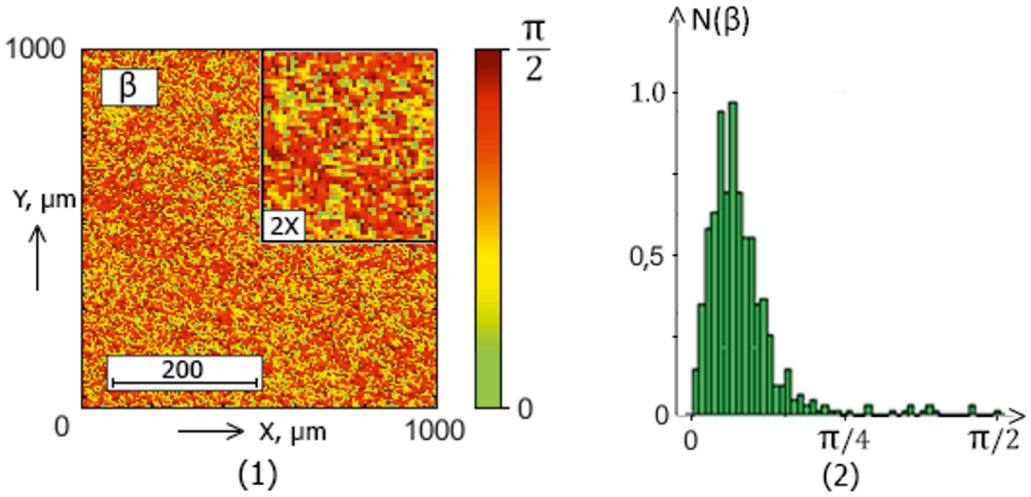

FIGURE 2
The blood facie polarization map [fragment (1)] and histogram [fragment (2)] for a patient from control group 1 (healthy donors).

transport it [62, 63] may be accompanied by an increase in the blood facies supramolecular protein networks phase anisotropy, which is taken from sick patients.

Our main attention will be focused on the object field single scattered component polarization maps $\beta(x,y)$ of blood facies from healthy donors and patients with various thyroid pathologies. We have shown (14, 15, 21) that this polarization parameter is determined by supramolecular networks phase-shifting properties or phase anisotropy.

5.1 Statistical analysis of polarization ellipticity maps

The series of Figures 2–5 presents the integral maps [fragments (1)] and ellipticity values distributions histograms [fragments (2)] of donors (control group 1) and patients with thyroid gland various pathologies (experimental groups 2–4).

The analysis of the obtained results revealed a correlation between the experimental data (Figures 2–5) and the proposed model of blood facies (patients in the control and study groups) speckle fields $H_{blood\,facie}(x,y)$ polarization structure formation (1–32). It was found that for all the considered pathologies (nodular goiter, autoimmune thyroiditis, papillary cancer), the blood facies samples object speckle fields have similar polarization ellipticity maps $\beta_{blood\,facie}(\vartheta_{xy})$ (fragments (1), Figures 2–5). This fact is illustrated by the histograms $N(\beta)$ of the polarization ellipticity value distributions (fragments (2), Figures 2–5). Each blood facies speckle field polarization map $\beta_{blood\,facie}(\vartheta_{xy})$ is characterized by a sufficiently wide range of change in the polarization ellipticity value ($0 \le \beta \le 0.5\pi$). Moreover, the probabilities of different ellipticity values formation (28, 29) of the donors and sick patients' blood facies samples speckle field (31, 32) are quite close in magnitude. At first glance, this experimental does not correspond to the proposed model scenario (1–23) of the polarization structure $\beta_{object}(\delta_{xy})$ formation and pathological transformation of the "object field" $E_{object}(x,y) \equiv \begin{pmatrix} E_x \\ E_y \\ \delta_{xy} \end{pmatrix}$ of blood facies optically anisotropic supramolecular networks (23). We have already noted that the architectonics $(\rho(x,y);\delta_{xy}(x,y))$ of such networks have a multilevel structure - nucleotide monomers, polypeptide protein chains, tertiary and quaternary structure of globular and fibrillar protein chains. When pathology occurs, the blood facies optical anisotropy (1–4) increases due to biochemical (*Tg* concentration increases) and conformational (structuring of globular and fibrillar protein networks). In terms of polarization, this should manifest itself in an increase in the magnitude and an increase in the range of change in the ellipticity values $\beta_{object}(\delta_{xy})$ (14, 15, 21, 22). However, in the multiple scattering presence in the blood facies volume, regardless of the presence and pathology type, along with the "object" $E_{object}(x,y) \equiv \begin{pmatrix} E_x \\ E_y \\ \delta_{xy} \end{pmatrix}$ (23) component, a "speckle" $U_{speckle}(x,y) \equiv \begin{pmatrix} U_x \\ U_y \\ \varphi_{xy} \end{pmatrix}$ (30) component is also formed. The interference mechanisms of such a component formation (24–30) transform and average the polarization ellipticity value $\beta_{object}(\delta_{xy})$ "object" distributions, individual for each pathology type. Due to such averaging, diagnostically significant differences between the polarization ellipticity $\beta_{object}(x,y,\delta_{xy})$ "object" maps are leveled. The fact is that each act of scattered waves $\tilde{E}_{xj}(r)$ and $\tilde{E}_{yj}(r)$ interference addition (24–26) changes the polarization ellipticity $\tilde{\beta}(x,y,\varphi_{x,y})$ value (28, 29). Moreover, the "interference" phase shifts $\varphi_{x,y}$ values (26) can significantly exceed similar "object" parameters $\delta_{x,y}$ (15). Due to this, the secondary interference influence on the donors and sick patients' blood facies polarization ellipticity

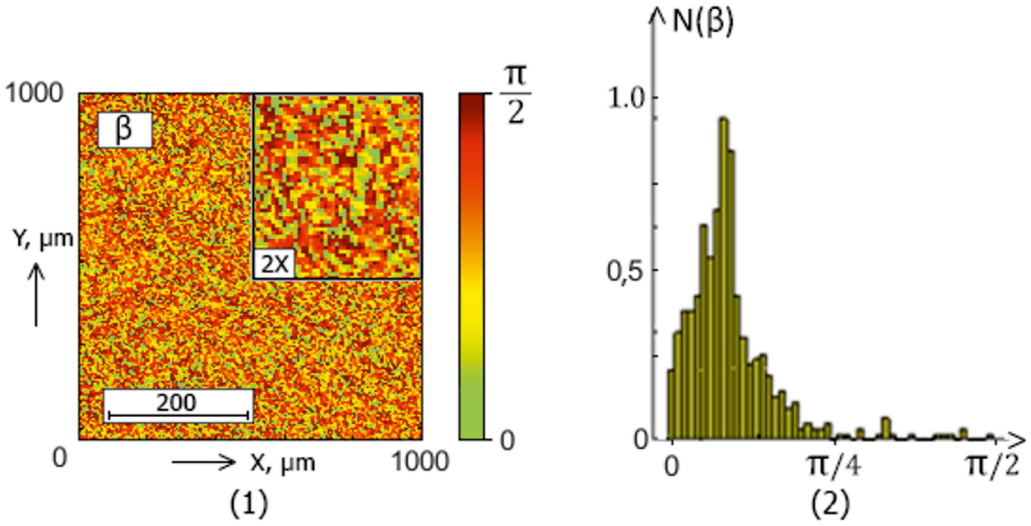

FIGURE 3
The blood facie polarization map [fragment (1)] and histogram [fragment (2)] for a patient from experimental group 2 (patients with nodular goiter).

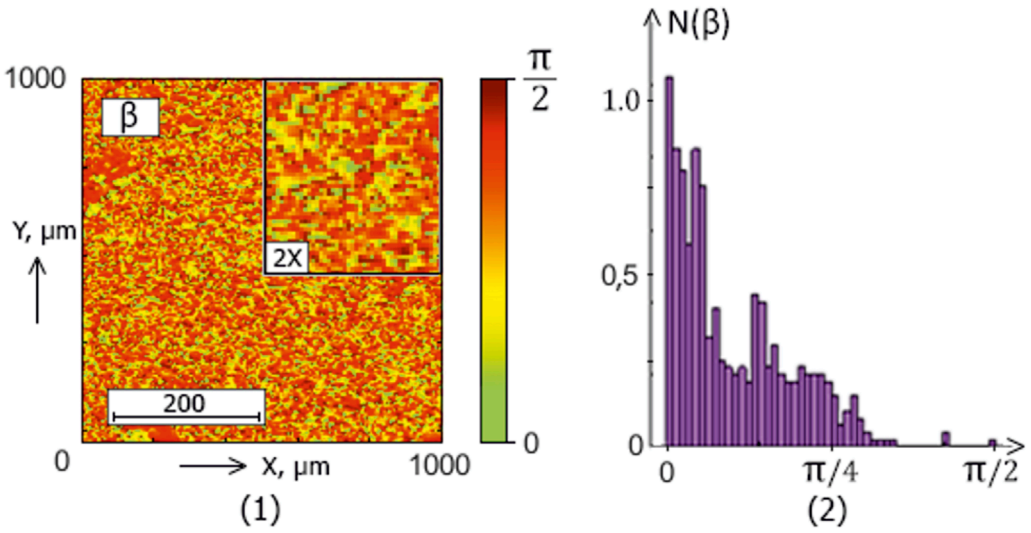

FIGURE 4
The blood facie polarization map [fragment (1)] and histogram [fragment (2)] for a patient from experimental group 3 (patients with autoimmune thyroiditis).

$\beta_{speckle}(x,y,\varphi_{xy})$ maps formation becomes decisive. The random ellipticity values distributions statistical analysis results illustrate the quantitative similarity of the blood facies speckle fields polarization structure for all groups (38), - Table 2.

A statistical test based on the Mann-Whitney test was used for pairwise comparisons of polarization ellipticity random values from statistically independent samples. The comparisons were made between the following groups: group 1 vs. group 2, group 1 vs. group 3, group 1 vs. group 4, group 2 vs. group 3, group 2 vs. group 4, and group 3 vs. group 4.

The statistical analysis results revealed:

- Statistically insignificant ($p_{12;13;14} > 0.05$; $p_{23;24;34} > 0.05$) increase in the average SM_1 of the distribution $\beta(m,n)$ statistical value within individual representative samples the from 0.187 to 0.22.
- The $\beta(m,n)$ distributions dispersion SM_2 value also turned out to be statistically insignificant ($p_{12;13;14} > 0.05$; $p_{23;24;34} > 0.05$) in the range from 0.082 to 0.123.
- The 3rd-order SM_3 statistical moment, which characterizes the $\beta(m,n)$ distributions skewness and varies from 0.66 to 0.89, was also found to be statistically insignificant for differential diagnosis.

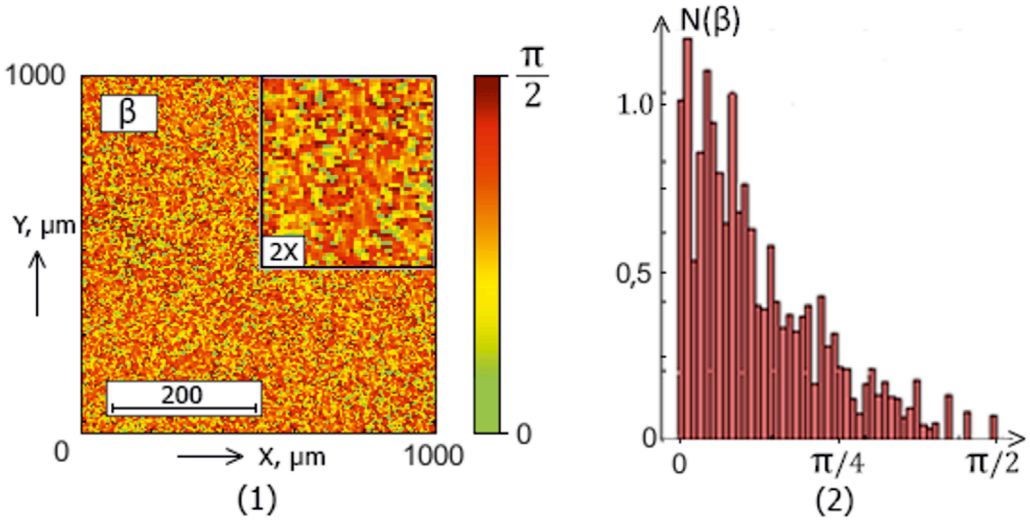

FIGURE 5
The blood facie polarization map [fragment (1)] and histogram [fragment (2)] for a patient from experimental group 4 (patients with papillary cancer).

TABLE 2 Donors and patients with various thyroid gland pathologies blood facies polarization ellipticity maps statistical parameters.

Groups	Group 1 (51 samples)	Group 2 (51 samples)	Group 3 (51 samples)	Group 4 (51 samples)
Average, SM_1	0.187 ± 0.01	0.205 ± 0.01	0.212 ± 0.01	0.22 ± 0.01
p_{ik}	$p_{12;13;14} > 0.05$			
	$p_{23;24;34} > 0.05$			
Dispersion, SM_2	0.082 ± 0.005	0.093 ± 0.006	0.114 ± 0.007	0.123 ± 0.008
p_{ik}	$p_{12;13;14} > 0.05$			
	$p_{23;24;34} > 0.05$			
Asymmetry, SM_3	0.89 ± 0.05	0.78 ± 0.04	0.71 ± 0.04	0.66 ± 0.04
p_{ik}	$p_{12;13;14} > 0.05$			
	$p_{23;24;34} > 0.05$			
Kurtosis, SM_4	1.47 ± 0.09	1.18 ± 0.06	0.94 ± 0.06	0.83 ± 0.05
p_{ik}	$p_{12;13;14} < 0.05$			
	$p_{23;24;34} > 0.05$			

- The blood facies polarization maps sensitivity to intergroup changes has kurtosis SM_4 of the ellipticity random values distributions.
- Kurtosis SM_4 varies statistically significantly ($p_{12;13;14} \leq 0.05$) from 0.83 to 1.47 and can be used as a marker for detecting the presence of thyroid gland pathology.

Therefore, for different pathologies ("normal - nodular goiter - autoimmune thyroiditis - papillary cancer"), the polarization ellipticity $\beta(m,n)$ distributions mean and dispersion change slightly. Also, the 3rd and 4th orders statistical moments changes in intergroup differences between which reach 30%–40%, turned out to be insufficiently sensitive.

To assess the diagnostic power of the method of polarization-interference mapping of laser speckle fields of blood facies, we used a number of evidence-based medicine operational characteristics[36] - sensitivity ($Se = \frac{A}{N}100\%$); specificity ($Sp = \frac{B}{T}100\%$) and accuracy ($Ac = \frac{A+B}{N+T}100\%$). Here A - diagnostic method among all samples from experimental group 2 (N) correct positive results; B - correct negative results of the method among control group 1 (T). If $(N+T) = (A+B)$, then Ac is called balanced accuracy.

In our work, the following scale for evaluating the diagnostic accuracy Ac is used:

- Unsatisfactory - ≤ 70%;
- Satisfactory – 71%–80%;
- Good – 81%–85%;
- Very good – 86%–90%;
- Excellent - > 90%.

The thyroid gland pathology differential diagnosis balanced accuracy [76] results are systematized in Table 3. Here a - is the correct results total number among all samples according to control group 1 and sequentially to experimental groups 2 (nodular goiter), 3 (autoimmune thyroiditis) and 4 (papillary cancer); b - is the false positives total number among all samples according to all groups.

The information analysis results demonstrated a slight diagnostic capacity for diagnosing and differentiating thyroid pathology (control group 1 and the set of all experimental groups "2–4″) - all statistical markers do not provide a balanced accuracy value higher than 80%.

A different situation is realized when using blood facies speckle fields $\begin{pmatrix} H_x; \\ H_y; \\ \vartheta_{xy} \end{pmatrix}$ polarization-interference mapping with phase scanning (35–37) and polarization ellipticity $\beta_{blood\ facie}\left(\Delta\theta_{xy} \rightarrow \vartheta_{xy}\right)$ layered maps digital algorithmic reconstruction (21, 28, 34).

The series Figures 6–9 illustrates the algorithmically obtained in the phase plane $(\theta_k = \frac{\pi}{8})$ "object" component $\begin{pmatrix} E_x; \\ E_y; \\ \delta_{xy} \end{pmatrix}$ polarization ellipticity $\beta_{object}(\theta_k, x, y)$ maps in donors and sick patients' blood facies speckle fields $\begin{pmatrix} H_x; \\ H_y; \\ \vartheta_{xy} \end{pmatrix}$. The value $(\theta_k = \frac{\pi}{8})$ is established by step-by-step $(\Delta\theta_{xy})$ phase scanning and algorithmically reconstructed polarization ellipticity value distributions $\beta_{speckle}\left(\Delta\theta_{xy}, x, y\right)$ statistical analysis. The phase plane $(\theta_k = \frac{\pi}{8})$ corresponds to the statistical criterion $SM_{g=1;2;3;4}\left(\beta\left(\Delta\theta_{xy} \le \theta_k\right)\right) \approx const$ for determining the single scattered "object" component $\begin{pmatrix} E_x; \\ E_y; \\ \delta_{xy} \end{pmatrix}$. "Object" polarization maps $\beta_{object}(\theta_k, x, y)$ (fragments (1), Figures 6–9) comparative analysis revealed a significant decrease in the interval ellipticity value β_{object} change in comparison with "speckle" distributions $\beta_{speckle}\left(\vartheta_{xy}, x, y\right)$, - fragments (1), Figures 2–5. This confirms the algorithmic elimination of the scattered component $\beta_{speckle}\left(\varphi_{xy}, x, y\right)$ distorting influence on the "object" ellipticity coordinate distributions (6–8, 10, 11, 14–16, 21, 22). In accordance with the presented blood facies optical anisotropy model concepts (1–5), it is possible to estimate the most probable changes in the singly scattered component $\begin{pmatrix} E_x; \\ E_y; \\ \delta_{xy} \end{pmatrix}$ polarization ellipticity value. It is known [58] that the protein structures' birefringence value corresponds to the level $(\Delta n \sim 1.5 \times 10^{-3})$; the blood facies geometric thickness l varies within the range from $30\mu m$ to $100\mu m$; the laser radiation wavelength $\lambda = 0.6328\mu m$. Assuming that the blood facies' entire volume is birefringent, the "object" phase shift value δ_{xy} fluctuates in variation range within the limits from $\frac{\pi}{6}$ to $\frac{\pi}{2}$. Based on this and the single scattered laser

TABLE 3 Thyroid pathology differential diagnosis balanced accuracy.

Average, SM_1		
$a = 70$	$a = 71$	$a = 72$
$b = 32$	$b = 31$	$b = 30$
$Ac_{12} = 68.6\%$	$Ac_{13} = 69.6\%$	$Ac_{14} = 70.6\%$
$a = 70$	$a = 70$	$a = 71$
$b = 32$	$b = 32$	$b = 31$
$Ac_{23} = 68.6\%$	$Ac_{24} = 68.6\%$	$Ac_{34} = 69.6\%$
Dispersion, SM_2		
$a = 72$	$a = 73$	$a = 74$
$b = 30$	$b = 29$	$b = 28$
$Ac_{12} = 70.6\%$	$Ac_{13} = 71.5\%$	$Ac_{14} = 72.5\%$
$a = 71$	$a = 72$	$a = 73$
$b = 31$	$b = 30$	$b = 29$
$Ac_{23} = 69.6\%$	$Ac_{24} = 70.6\%$	$Ac_{34} = 71.6\%$
Asymmetry, SM_3		
$a = 75$	$a = 76$	$a = 77$
$b = 27$	$b = 26$	$b = 25$
$Ac_{12} = 73.5\%$	$Ac_{13} = 74.5\%$	$Ac_{14} = 75.5\%$
$a = 73$	$a = 74$	$a = 75$
$b = 29$	$b = 28$	$b = 27$
$Ac_{23} = 71.5\%$	$Ac_{24} = 72.5\%$	$Ac_{34} = 73.5\%$
Kurtosis, SM_4		
$a = 76$	$a = 77$	$a = 78$
$b = 26$	$b = 25$	$b = 24$
$Ac_{12} = 74.5\%$	$Ac_{13} = 75.5\%$	$Ac_{14} = 76.5\%$
$a = 74$	$a = 75$	$a = 76$
$b = 28$	$b = 27$	$b = 26$
$Ac_{23} = 72.5\%$	$Ac_{24} = 73.5\%$	$Ac_{34} = 74.5\%$

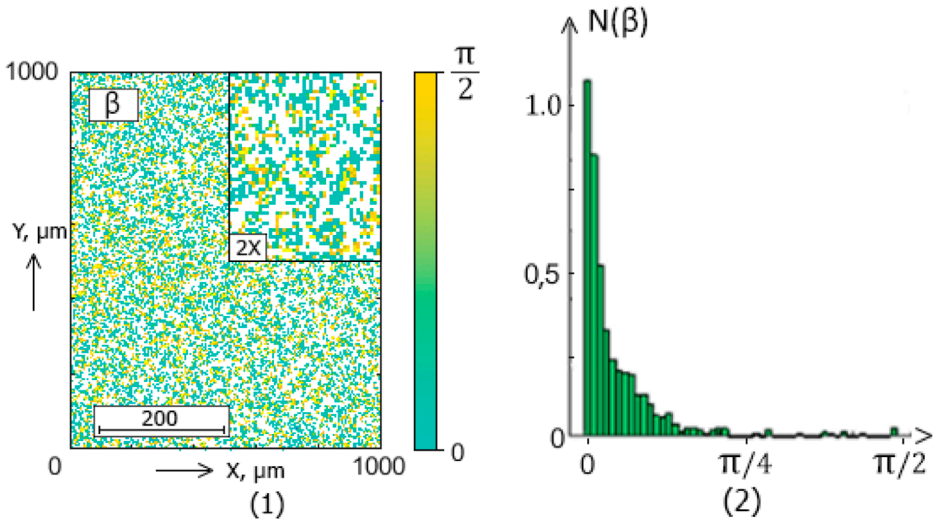

FIGURE 6
The blood facie phase ($\theta_k = \frac{\pi}{8}$) polarization map [fragment (1)] and histogram [fragment (2)] for a patient from control group 1 (healthy donors).

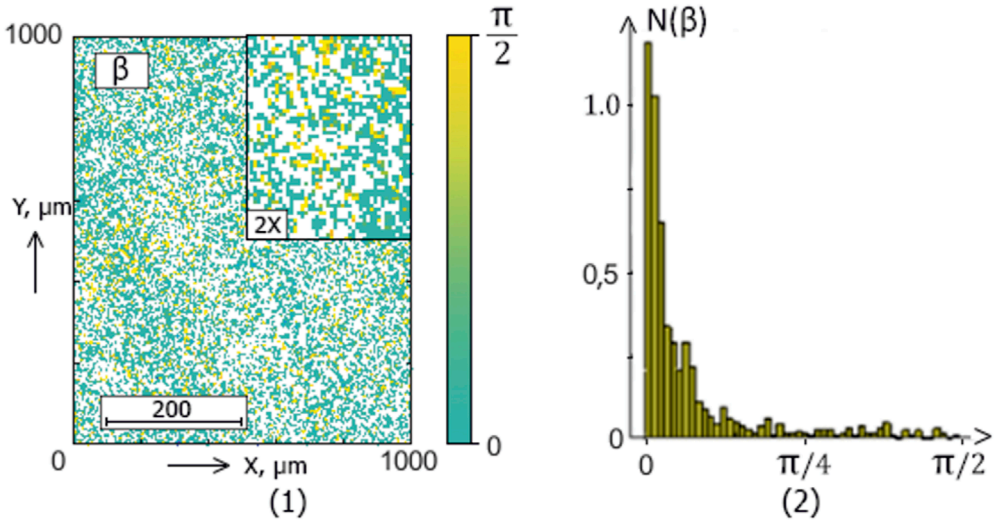

FIGURE 7
The blood facie phase ($\theta_k = \frac{\pi}{8}$) polarization map [fragment (1)] and histogram [fragment (2)] for a patient from experimental group 2 (patients with nodular goiter).

waves $\begin{pmatrix} E_x; \\ E_y; \\ \delta_{xy} \end{pmatrix}$ formation conditions (10, 11, 14, 15, 21, 22), the maximum $\frac{\pi}{4}$ ellipticity β_{object} level formation is probable. However, for real blood facies experimental samples, polarization states with a significantly lower ellipticity value (fragments (2), Figures 6–9) are more probable. The noted fact can be explained by the fact that optically anisotropic supramolecular networks are spatially structured and do not fill the blood facies volume. As a result, the birefringent globular and fibrillar protein chains effective geometric dimensions $l_{effective}$ decrease. As a result, the "object" phase shifts δ_{xy} and ellipticity β_{object} values (15, 21) are concentrated in a "narrower" range–from 0 to $\frac{\pi}{4}$.

The ellipticity distributions $\beta_{object}(\theta_k, x, y)$ histograms $N(\beta)$ comparative analysis in the phase plane ($\theta_k = \frac{\pi}{8}$) revealed a tendency for its value to consistently increase for the blood facies of donors [Figure 6, fragment (2)] and patients with nodular goiter [Figure 7, fragment (2)], autoimmune thyroiditis [Figure 8, fragment (2)], and papillary cancer [Figure 9, fragment (2)]. This fact is indicated by a decrease in the histogram kurtosis (SM_4) due to a reduction in the polarization ellipticity β_{object} minimum values. At the same time, the probability distributions $N(\beta)$ of the polarization parameter become more symmetrical–skewness value SM_3 decreases. The

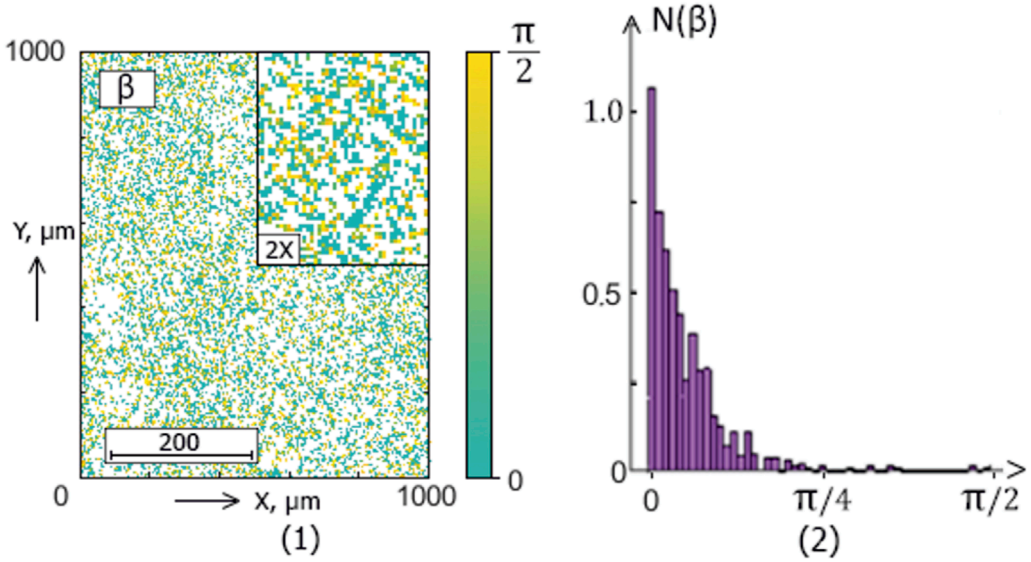

FIGURE 8
The blood facie phase ($\theta_k = \frac{\pi}{8}$) polarization map [fragment (1)] and histogram [fragment (2)] for a patient from experimental group 3 (patients with autoimmune thyroiditis).

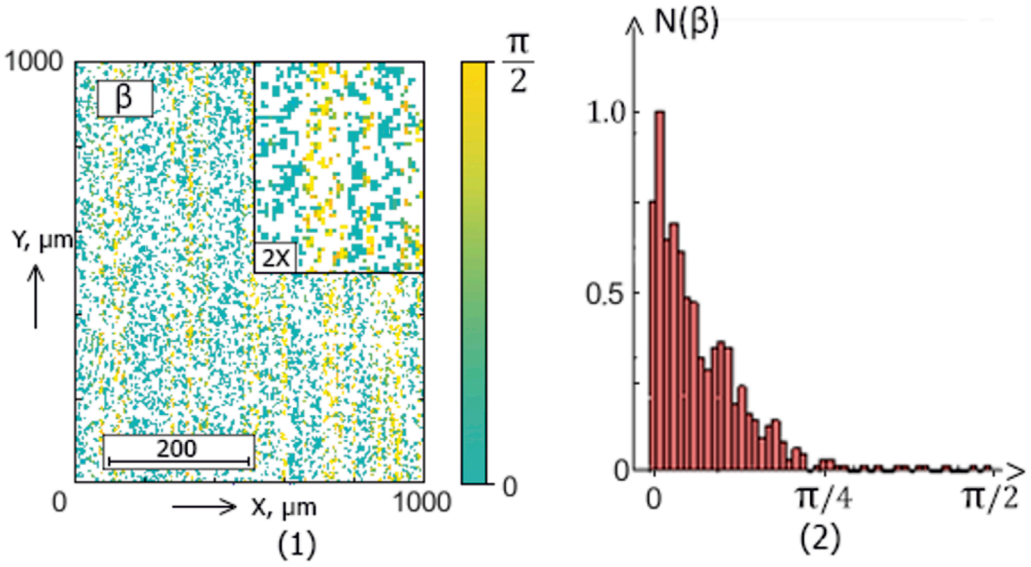

FIGURE 9
The blood facie phase ($\theta_k = \frac{\pi}{8}$) polarization map [fragment (1)] and histogram [fragment (2)] for a patient from experimental group 4 (patients with papillary cancer).

revealed scenario of "pathological" transformation of blood facies speckle field $\begin{pmatrix} H_x; \\ H_y; \\ \vartheta_{xy} \end{pmatrix}$ "object" component $\begin{pmatrix} E_x; \\ E_y; \\ \delta_{xy} \end{pmatrix}$ ellipticity maps $\beta_{object}(\theta_k, x, y)$ correlates with the proposed optical anisotropy model of supramolecular networks (1–4). According to the specified model, pathological conditions (from nodular goiter, and autoimmune thyroiditis to papillary cancer) are manifested in a consistent increase in the value and increase in the range of change in ellipticity (14, 15, 21, 22) due to biochemical (increasing *Tg* concentration) and conformational (structuring of globular and fibrillar protein networks).

Within the framework of the statistical approach (38), such pathological transformations should be accompanied by an increase in the mean (SM_1) and dispersion (SM_2) values, which characterize the polarization maps $\beta_{object}(\theta_k, x, y)$. The higher-order

TABLE 4 Blood facies polarization ellipticity phase maps statistical parameters.

Groups	Group 1 (51 samples)	Group 2 (51 samples)	Group 3 (51 samples)	Group 4 (51 samples)
Average, SM_1	0.15 ±0.008	0.17 ±0.009	0.185 ±0.01	0.194 ±0.01
p_{ik}	$p_{12;13;14} \le 0.05$;			
	$p_{23;24;34} \le 0.05$			
Dispersion, SM_2	0.069 ±0.004	0.081 ±0.005	0.096 ±0.006	0.11 ±0.007
p_{ik}	$p_{12;13;14} \le 0.05$			
	$p_{23;24;34} \le 0.05$			
Skewness, SM_3	1.21 ±0.07	0.99 ±0.05	0.88 ±0.05	0.81 ±0.04
p_{ik}	$p_{12;13;14} \le 0.001$			
	$p_{23;24;34} \le 0.05$			
Kurtosis, SM_4	2.07 ±0.1	1.79 ±0.1	1.54 ±0.08	1.22 ±0.07
p_{ik}	$p_{12;13;14} \le 0.001$			
	$p_{23;24;34} \le 0.05$			

statistical moments $SM_{3;4}$ values, $SM_3 \sim \frac{1}{(SM_2)^3}$ and $SM_4 \sim \frac{1}{(SM_2)^4}$, should decrease.

This scenario of the difference's formation between the blood facies polarization "object" maps $\beta_{object}(\theta_k, x, y)$ from all groups is confirmed by the 1st – 4th orders central statistical moments $SM_{g=1;2;3;4}$ calculation, - Table 4.

Polarization ellipticity maps $\beta_{object}(\theta_k, x, y)$ statistical analysis revealed:

Statistical significance for diagnostics ($p_{12;13;14}$) and differentiation ($p_{23;24;34}$) of entire set thyroid pathology markers.

The mean SM_1 and dispersion SM_2 are statistically significant ($p_{ik} < 0.05$) and consistently (from control group 1 to experimental groups 2–4) increase within - $SM_1 \sim from\, 0.15\, to\, 0.194$ and $SM_2 \sim from\, 0.069\, to\, 0.11$.

Skewness SM_3 and kurtosis SM_4 have statistically reliable diagnostic ($p_{12;13;14} < 0.001$) and differentiation ($p_{23;24;34} < 0.05$) sensitivity to changes in the layered maps $\beta_{object}(\theta_k, x, y)$ structure.

The polarization ellipticity β_{object} values distributions skewness SM_3 magnitude vary from 1.21 to 0.81; The kurtosis SM_4, which characterizes the peak sharpness of the blood facies speckle field $\begin{pmatrix} H_x; \\ H_y; \\ \vartheta_{xy} \end{pmatrix}$ single scattered component $\begin{pmatrix} E_x; \\ E_y; \\ \delta_{xy} \end{pmatrix}$ polarization distributions $\beta_{object}(\theta_k, x, y)$, consistently decreases from 2.07 to 1.22.

The information analysis results (Table 5) revealed a significant increase (from "unsatisfactory" to "very good" and "excellent" levels) in sensitivity compared with integral ellipticity polarization mapping.

The following balanced accuracy levels were demonstrated for the differential diagnosis of thyroid gland pathologies:

1. Thyroid gland pathology diagnosis (control group 1 and all experimental groups "2–4"):

   - "normal - nodular goiter" $Ac_{12}(SM_3; SM_4) \sim 91.2\%$ - "excellent" level;
   - "normal - autoimmune thyroiditis" $Ac_{13}(SM_3; SM_4) \sim 92.1\%$ - "excellent" level;
   - "normal - papillary cancer" $Ac_{14}(SM_3; SM_4) \sim 93.1\%$ - "excellent" level.

2. Differential diagnosis:

   - "nodular goiter - autoimmune thyroiditis" $Ac_{23}(SM_3; SM_4) \sim 87\%$ - "very good" level;
   - "nodular goiter - papillary cancer" $Ac_{24}(SM_3; SM_4) \sim 88\%$ - "very good" level;
   - "autoimmune thyroiditis - papillary cancer" $Ac_{34}(SM_3; SM_4) \sim 89\%$ - "very good" level.

6 Research prospects

The proposed polarization-interference technique for phase scanning of blood facies speckle fields, using algorithmic selection of polarization ellipticity maps, will be improved by developing new digital holography algorithms. These algorithms will reconstruct maps of linear and circular birefringence as well as dichroism. This enhancement will expand the functional capabilities of the technique, increase the sensitivity of laser polarization-interference differential diagnostics, and open up new possibilities for objective screening and monitoring of thyroid disease treatment.

TABLE 5 Thyroid pathology differential diagnosis balanced accuracy.

Average, SM_1		
$a = 85$	$a = 88$	$a = 89$
$b = 17$	$b = 14$	$b = 13$
$Ac_{12} = 84.3\%$	$Ac_{13} = 86.3\%$	$Ac_{14} = 87.3\%$
$a = 80$	$a = 82$	$a = 83$
$b = 22$	$b = 20$	$b = 19$
$Ac_{23} = 78.4\%$	$Ac_{24} = 80.4\%$	$Ac_{34} = 81.4\%$
Dispersion, SM_2		
$a = 85$	$a = 88$	$a = 89$
$b = 17$	$b = 14$	$b = 13$
$Ac_{12} = 84.3\%$	$Ac_{13} = 86.3\%$	$Ac_{14} = 87.3\%$
$a = 80$	$a = 82$	$a = 83$
$b = 22$	$b = 20$	$b = 19$
$Ac_{23} = 78.4\%$	$Ac_{24} = 80.4\%$	$Ac_{34} = 81.4\%$
Skewness, SM_3		
$a = 93$	$a = 94$	$a = 95$
$b = 9$	$b = 8$	$b = 7$
$Ac_{12} = 91.2\%$	$Ac_{13} = 92,1\%$	$Ac_{14} = 93.1\%$
$a = 89$	$a = 90$	$a = 91$
$b = 13$	$b = 12$	$b = 11$
$Ac_{23} = 87.3\%$	$Ac_{24} = 88.2\%$	$Ac_{34} = 89.2\%$
Kurtosis, SM_4		
$a = 93$	$a = 94$	$a = 95$
$b = 9$	$b = 8$	$b = 7$
$Ac_{12} = 91.2\%$	$Ac_{13} = 92.1\%$	$Ac_{14} = 93.1\%$
$a = 89$	$a = 90$	$a = 91$
$b = 13$	$b = 12$	$b = 11$
$Ac_{23} = 87.3\%$	$Ac_{24} = 88.2\%$	$Ac_{34} = 89.2\%$

7 Conclusion

1. For the first time, a minimally invasive laser technique for polarization-interference layer-by-layer mapping of dehydrated blood films was developed and experimentally tested for the differential diagnosis of thyroid pathology.
2. To provide a physical basis and prognostic analysis of the polarization structure of speckle fields, a model description of the polycrystalline structure of supramolecular networks in blood facies was developed for the first time, using the approximation of linear and circular birefringence.
3. No statistically significant markers were identified through direct polarization-interference mapping and statistical analysis of measured "integral" maps of the ellipticity of the diffuse component of speckle fields in blood facies. As a result, the differential diagnosis of thyroid pathology did not exceed a satisfactory level of 80%.
4. Digital phase scanning of algorithmically reconstructed fields of complex amplitudes enabled the measurement of polarization ellipticity maps of the singly scattered component in the object speckle fields of blood facies. Based on this, new statistically significant markers for minimally invasive differential diagnosis of thyroid pathology were identified and physically substantiated.
5. The following results of differential diagnosis of thyroid pathology have been achieved:

5. 1. Thyroid gland pathology diagnosis (control group 1 and all experimental groups "2–4"):

- "normal - nodular goiter" $Ac_{12}(SM_3;SM_4) \sim 91.2\%$ - "excellent" level;
- "normal - autoimmune thyroiditis" $Ac_{13}(SM_3;SM_4) \sim 92.1\%$ - "excellent" level;
- "normal - papillary cancer" $Ac_{14}(SM_3;SM_4) \sim 93.1\%$ - "excellent" level.

5. 2. Differential diagnosis:

- "nodular goiter - autoimmune thyroiditis" $Ac_{23}(SM_3;SM_4) \sim 87\%$ - "very good" level;
- "nodular goiter - papillary cancer" $Ac_{24}(SM_3;SM_4) \sim 88\%$ - "very good" level;
- "autoimmune thyroiditis - papillary cancer" $Ac_{34}(SM_3;SM_4) \sim 89\%$ - "very good" level.

Data availability statement

The original contributions presented in the study are included in the article/supplementary material, further inquiries can be directed to the corresponding authors.

Ethics statement

The studies involving humans were approved by Ethics Committee of the Bukovinian State Medical University (Chernivtsi, Ukraine). The studies were conducted in accordance with the local legislation and institutional requirements. The participants provided their written informed consent to participate in this study. Written informed consent was obtained from the individual(s) for the publication of any potentially identifiable images or data included in this article.

Author contributions

OU: Conceptualization, Formal Analysis, Project administration, Validation, Writing–original draft, Writing–review and editing. OB: Conceptualization, Investigation, Writing–review and editing. JZ: Formal Analysis, Methodology, Writing–original draft. AD: Data curation, Investigation, Software, Visualization, Writing–review and editing. OO: Software, Writing–review and editing. YU: Conceptualization, Investigation, Project administration, Supervision, Writing–original draft. IS: Formal Analysis, Investigation, Methodology, Writing–review and editing. IM: Data curation, Writing–review and editing. VS: Conceptualization, Writing–review and editing. ZC: Formal Analysis, Methodology, Writing–review and editing.

Funding

The author(s) declare that financial support was received for the research, authorship, and/or publication of this article. Authors acknowledge the support from the National Research Foundation of Ukraine, Project 2022.01/0034; Project 2023.01/0174.

Conflict of interest

The authors declare that the research was conducted in the absence of any commercial or financial relationships that could be construed as a potential conflict of interest.

Publisher's note

All claims expressed in this article are solely those of the authors and do not necessarily represent those of their affiliated organizations, or those of the publisher, the editors and the reviewers. Any product that may be evaluated in this article, or claim that may be made by its manufacturer, is not guaranteed or endorsed by the publisher.

References

1. Tuchin VV. Tissue optics and photonics: light-tissue interaction. *J Biomed Photon Eng* (2015) 1:98–134. doi:10.18287/jbpe-2015-1-2-98

2. Vo-Dinh T. *Biomedical photonics handbook*. Boca Raton: CRC Press (2014). p. 850.

3. Boas DA, Pitris C, Ramanujam N. *Handbook of biomedical optics*. Boca Raton: CRC Press (2011). p. 831.

4. Valery V. Tuchin. Tissue optics: light scattering methods and instruments for medical diagnosis. In: *Tissue optics: light scattering methods and instruments for medical diagnosis*. 3rd ed. WA, USA: Society of Photo-Optical Instrumentation Engineers SPIE Ebooks (2015). doi:10.1117/3.1003040

5. Wang LV, Wu H-I. *Biomedical optics. Biomedical optics: principles and imaging*. John Wiley and Sons, Inc. (2009). p. 362.

6. Ushenko AG, Pishak VP. Laser polarimetry of biological tissues: principles and applications. In: VV Tuchin, editor. *Handbook of coherent domain optical methods*. Springer US (2004). p. 93–138.

7. Ghosh N. Tissue polarimetry: concepts, challenges, applications, and outlook. *J Biomed Opt* (2011) 16:110801. doi:10.1117/1.3652896

8. Jacques SL. Polarized light imaging of biological tissues. In: D Boas, C Pitris, N Ramanujam, editors. *Handbook of biomedical optics 2*. Boca Raton: CRC Press (2011). p. 649–69.

9. Ghosh N, Wood M, Vitkin A. Polarized light assessment of complex turbid media such as biological tissues using mueller matrix decomposition. In: VV Tuchin, editor. *Handbook of photonics for biomedical science*. Boca Raton: CRC Press (2010). p. 253–82.

10. Layden D, Ghosh N, Vitkin IA. Quantitative polarimetry for tissue characterization and diagnosis. In: RK Wang, VV Tuchin, editors. *Advanced biophotonics: tissue optical sectioning*. Boca Raton: CRC Press (2013). p. 73–108.

11. Vitkin A, Ghosh N, de Martino A Tissue polarimetry. in *Photonics: scientific foundations, Technology and applications. In:* ed. DL Andrews editor. John Wiley and Sons, Ltd. (2015). p. 239–321.

12. Tuchin VV. Tissue optics and photonics: biological tissue structures. *J Biomed Photon Eng* (2015) 1:3–21. doi:10.18287/jbpe-2015-1-1-3

13. Bai X, Liang Z, Zhu Z, Schwing A, Forsyth D, Gruev V. Polarization-based underwater geolocalization with deep learning. *eLight* (2023) 3:15. doi:10.1186/s43593-023-00050-6

14. Lee HR, Lotz C, Kai Groeber Becker F, Dembski S, Novikova T. Digital histology of tissue with Mueller microscopy and FastDBSCAN. *Appl Opt* (2022) 61(32):9616–24. doi:10.1364/ao.473095

15. Kim M, Lee HR, Ossikovski R, Malfait-Jobart A, Lamarque D, Novikova T. Optical diagnosis of gastric tissue biopsies with Mueller microscopy and statistical analysis. *J Europ Opt Soc Rapid Publ* (2022) 18(2):10. doi:10.1051/jeos/2022011

16. Lee HR, Li P, Yoo TSH, Lotz C, Groeber-Becker FK, Dembski S, et al. Digital histology with Mueller microscopy: how to mitigate an impact of tissue cut thickness fluctuations. *J Biomed Opt* (2019) 24(7):1. doi:10.1117/1.jbo.24.7.076004

17. Li P, Lee HR, Chandel S, Lotz C, Groeber-Becker FK, Dembski S, et al. Analysis of tissue microstructure with Mueller microscopy: logarithmic decomposition and Monte Carlo modeling. *J Biomed Opt* (2020) 25(1):1. doi:10.1117/1.jbo.25.1.015002

18. Lee HR, Yoo TSH, Li P, Lotz C, Groeber-Becker FK, Dembski S, et al. Mueller microscopy of anisotropic scattering media: theory and experiments. *Proc SPIE 10677 Unconventional Opt Imaging* (2018) 10677.

19. Ma H, He H, Ramella-Roman JC. Mueller matrix microscopy. In: JC Ramella-Roman, T Novikova, editors. *Polarized light in biomedical imaging and sensing*. Cham: Springer (2023). p. 281–321.

20. Ushenko YA, Koval GD, Ushenko AG, Dubolazov OV, Ushenko VA, Novakovskaia OY. Mueller-matrix of laser-induced autofluorescence of polycrystalline films of dried peritoneal fluid in diagnostics of endometriosis. *J Biomed Opt* (2016) 21(7):071116. doi:10.1117/1.jbo.21.7.071116

21. Angelsky PO, Ushenko AG, Dubolazov AV, Sidor MI, Bodnar GB, Koval G, et al. The singular approach for processing polarization-inhomogeneous laser images of blood plasma layers. *J Opt* (2013) 15(4):044030. doi:10.1088/2040-8978/15/4/044030

22. Angelsky OV, Ushenko AG, Pishak VP, Burkovets DN, Yermolenko SB, Pishak O, et al. Coherent introscopy of phase-inhomogeneous surfaces and layers. *Photon Devices, Syst* (1999) 4016:413–8. doi:10.1117/12.373664

23. Ushenko AG, Dubolazov AV, Ushenko VA, Novakovskaya OY. Statistical analysis of polarization-inhomogeneous Fourier spectra of laser radiation scattered by human skin in the tasks of differentiation of benign and malignant formations. *J Biomed Opt* (2016) 21(7):071110. doi:10.1117/1.jbo.21.7.071110

24. Yermolenko S, Ushenko A, Ivashko P, Gruia I, Zimnyakov D, Gavrila C, et al. Spectropolarimetry of cancer change of biotissues. *Ninth Int Conf Correlation Opt* (2009) 7388:404–10.

25. Ushenko VA, Hogan BT, Dubolazov A, Grechina AV, Boronikhina TV, Gorsky M, et al. Embossed topographic depolarisation maps of biological tissues with different morphological structures. *Scientific Rep* (2021) 11(1):3871. doi:10.1038/s41598-021-83017-2

26. Olar EI, Ushenko AG, Ushenko YA. Correlation microstructure of the Jones matrices for multifractal networks of biotissues. *Laser Phys* (2004) 14(7):1012–8.

27. Ushenko A, Sdobnov A, Dubolazov A, Grytsiuk M, Ushenko Y, Bykov A, et al. Stokes-correlometry analysis of biological tissues with polycrystalline structure. *IEEE J Selected Top Quan Electronics* (2018) 25(1):1–12. doi:10.1109/jstqe.2018.2865443

28. Angelsky OV, Ushenko AG, Zenkova CY, Felde CV, et al. *Optical measurements: polarization and coherence of light fields*. Rijeka, Croatia: INTECH Open Access Publisher (2012).

29. Pishak VP, Ushenko AG, Gryhoryshyn P, et al. Polarization structure of biospeckle fields in crosslinked tissues of a human organism: 1. Vector structure of skin biospeckles. *Int Conf Correlation Opt* (1997) 3317:418–24. Available from: https://iris.who.int/handle/10665/91976.

30. Eftimie LG, Glogojeanu RR, Tejaswee A, Gheorghita P, Stanciu SG, Chirila A, et al. Differential diagnosis of thyroid nodule capsules using random forest guided

selection of image features. *Scientific Rep* (2022) 12:21636. Article number: 21636. doi:10.1038/s41598-022-25788-w

31. Yang W-T, Ma B-Y, Chen Y. A narrative review of deep learning in thyroid imaging: current progress and future prospects. *Quant Imaging Med Surg* (2024) 14(2):2069–88. doi:10.21037/qims-23-908

32. Tokarz D, Cisek R, Joseph A, Asa SL, Wilson BC, Barzda V. Characterization of pathological thyroid tissue using polarization-sensitive second harmonic generation microscopy. *Lab Invest* (2020) 100(10):1280–7. doi:10.1038/s41374-020-0475-7

33. Richard C, Ariana JMA, Harvey DT. Polarization-sensitive second harmonic generation microscopy for investigations of diseased collagenous tissues. *Front Phys*. Sec. Optics and Photonics Volume 9 - 2021. doi:10.3389/fphy.2021.726996

34. Hristu R, Eftimie LG, Stanciu SG, Tranca DE, Paun B, Sajin M, et al. Quantitative second harmonic generation microscopy for the structural characterization of capsular collagen in thyroid neoplasms. *Biomed Opt Express* (2018) 9(8):3923–36. doi:10.1364/BOE.9.003923

35. de Boer JF, Milner TE. Review of polarization sensitive optical coherence tomography and Stokes vector determination. *J Biomed Opt* (2002) 7(3):359–71. doi:10.1117/1.1483879

36. K US, Mahato KK, Mazumder N. Polarization-resolved Stokes-Mueller imaging: a review of technology and applications. *Lasers Med Sci* (2019) 34(7):1283–93. doi:10.1007/s10103-019-02752-1

37. He Y, Li K, Li W, Qiu Y, Li D, Wang C, et al. Polarization coherency matrix tomography. *J Biophotonics* (2023) 16(9):e202300093. doi:10.1002/jbio.202300093

38. Yang D, Yuan Z, Hu M, Liang Y. Zebrafish brain and skull imaging based on polarization-sensitive optical coherence tomography. *J Biophotonics* (2022) 15(12):e202200112. doi:10.1002/jbio.202200112

39. Park JE, Xin Z, Kwon DY, Kim SW, Lee H, Jung MJ, et al. Application of polarization sensitive-optical coherence tomography to the assessment of phase retardation in subpleural cancer in rabbits. *Tissue Eng Regen Med* (2021) 18(1):61–9. doi:10.1007/s13770-020-00318-9

40. Willemse J, Gräfe MGO, Verbraak FD, de Boer JF. *In vivo* 3D determination of peripapillary scleral and retinal layer architecture using polarization-sensitive optical coherence tomography. *Transl Vis Sci Technol* (2020) 9(11):21. doi:10.1167/tvst.9.11.21

41. Baumann B, Augustin M, Lichtenegger A, Harper D, Muck M, Eugui P, et al. Polarization-sensitive optical coherence tomography imaging of the anterior mouse eye. *J Biomed Opt* (2018) 23(8):1–12. doi:10.1117/1.JBO.23.8.086005

42. Hariri LP, Adams DC, Applegate MB, Miller AJ, Roop BW, Villiger M, et al. Distinguishing tumor from associated fibrosis to increase diagnostic biopsy yield with polarization-sensitive optical coherence. *Tomography Clin Cancer Res* (2019) 25(17):5242–9. doi:10.1158/1078-0432.CCR-19-0566

43. Tao K, Sun K, Ding Z, Ma Y, Kuang H, Zhao H, et al. Catheter-based polarization sensitive optical coherence tomography using similar mueller matrix method. *IEEE Trans Biomed Eng* (2020) 67(1):60–8. doi:10.1109/TBME.2019.2908031

44. de Boer JF, Hitzenberger CK, Yasuno Y. Polarization sensitive optical coherence tomography – a review [Invited]. *tomography Biomed Opt Express* (2017) 8(Issue 3):1838–73. doi:10.1364/boe.8.001838

45. Peyvasteh M, Tryfonyuk L, Ushenko V, Syvokorovskaya AV, Dubolazov A, Vanchulyak O, et al. 3D Mueller-matrix-based azimuthal invariant tomography of polycrystalline structure within benign and malignant soft-tissue tumours. *Laser Phys Lett (2020)* (2020) 17(11):115606. doi:10.1088/1612-202x/abbee0

46. Ushenko AG, Dubolazov AV, Litvinenko OY, Bachinskiy VT, Bin L, Bin G, et al. 3D polarization correlometry of object fields of networks of biological crystals. *Proc SPIE* (2020) 11369:113691M.

47. Bodnar A, Dubolazov A, Pavlyukovich A, Pavlyukovichv N, Ushenko A, Motrich A, et al. 3D Stokes correlometry of the polycrystalline structure of biological tissues. *Proc SPIE* (2020) 11509:115090V.

48. Ushenko A, Dubolazov A, Zheng J, Bakun O, Gorsky M, Ushenko Y, et al. Mueller matrix polarization interferometry of optically anisotropic architectonics of biological tissue object fields: the fundamental and applied aspects. *Front Phys* (2024) 11:1302254. doi:10.3389/fphy.2023.1302254

49. Sdobnov A, Ushenko VA, Trifonyuk L, Bakun O, Garazdyuk M, Soltys IV, et al. Mueller-matrix imaging polarimetry elevated by wavelet decomposition and polarization-singular processing for analysis of specific cancerous tissue pathology. *J Biomed Opt* (2023) 28(10):102903. doi:10.1117/1.jbo.28.10.102903

50. Ushenko A, Zheng J, Gorsky M, Dubolazov A, Ushenko Y, Soltys I, et al. 3D digital holographic polarimetry of diffuse optically anisotropic biological tissue object fields. *Front Phys 111288935*.

51. Ushenko A, Zheng J, Litvinenko A, Gorsky M, Wanchuliak O, Dubolazov O, et al. 3D digital polarization-holographic wavelet histology in determining the duration of mechanical damage to the myocardium. *J Biophotonics* (2024) 17(3):e202300372. doi:10.1002/jbio.202300372

52. Ushenko A, Dubolazov A, Zheng J, Litvinenko A, Gorsky M, Ushenko Y, et al. 3D polarization-interference holographic histology for wavelet-based differentiation of the polycrystalline component of biological tissues with different necrotic states. Forensic applications. *J Biomed Opt* (2024) 29(5):052920. doi:10.1117/1.jbo.29.5.052920

53. Hunter R. *Foundations of colloid science/R. Hunter*. New York: Oxford University Press (2004). p. 806.

54. Chen X, Chen PG, Ouazzani J Numerical simulations of sessile droplet evaporating on heated substrate/X. *J Ouazzani//Eur Phys J Spec Top* (2017) 226(6):1325–35.

55. Dash S. Droplet evaporation on heated hydrophobic and superhydrophobic surfaces/S. *S.V Garimella//Phys Rev E* (2014) 89:1–8.

56. Gleason K. Microdroplet evaporation with a forced pinned contact line/K. Gleason, S.A. *Putnam//Langmuir: ACS J Surf Colloids* (2014) 30(34):10548–55.

57. Hu H, Larson RG, Hu RG. Evaporation of a sessile droplet on a substrate/H. *Larson//The J Phys Chem B* (2020) 106:1334–44.

58. Vladmir Z, Wang JB, Yan XH. Human blood plasma crystal and molecular biocolloid textures – dismetabolism and genetic breaches. *Nat Sci J – Xiangtan Univ* (2001) 23:118–27.

59. Abe S, Tanaka J, Kojima M, Kanamaru S, Hirata K, Yamashita K, et al. Cell-free protein crystallization for nanocrystal structure determination. *Scientific Rep* (2022) 12:16031. Article number: 16031. doi:10.1038/s41598-022-19681-9

60. Van den Beld AW, Kaufman JM, Zillikens MC, Lamberts SWJ, Egan JM, van der Lely AJ. The physiology of endocrine systems with ageing. *Lancet Diabetes Endocrinol* (2018) 6(8):647–58. doi:10.1016/S2213-8587(18)30026-3

61. Asa SL, Erickson LA, Rindi G. The spectrum of endocrine pathology. *Endocr Pathol* (2023) 34(4):368–81. doi:10.1007/s12022-023-09758-0

62. Brix K, Szumska J, Weber J, Qatato M, Venugopalan V, Al-Hashimi A, et al. Auto-regulation of the thyroid gland beyond classical pathways. *Exp Clin Endocrinol Diabetes* (2020) 128(6-07):437–45. doi:10.1055/a-1080-2969

63. Grieco G, Wang T, Delcorte O, Spourquet C, Janssens V, Strickaert A, et al. Class III PI3K Vps34 controls thyroid hormone production by regulating thyroglobulin iodination. *Lysosomal Proteolysis, Tissue Homeostasis Thyroid* (2020) 30(1):133–46. doi:10.1089/thy.2019.0182

64. Walter F. *PhD. Boron. Medical physiology: a cellular and molecular approaoch*. Elsevier/Saunders (2003). p. 1300. ISBN 1-4160-2328-3.

65. Delom F, Mallet B, Carayon P, Lejeune PJ. Role of extracellular molecular chaperones in the folding of oxidized proteins. Refolding of colloidal thyroglobulin by protein disulfide isomerase and immunoglobulin heavy chain-binding protein. *J Biol Chem Journal — United States* (2001) 276(24):21337–42. —ISSN 0021-9258. doi:10.1074/jbc.M101086200

66. Wagner I, Musso H 1983, New naturally occurring amino acids *Angew Chem Int Edition English : magazin.— 1983.— November (Bd. 22,Nr. 11)*.—S. 22, 816–28.doi:10.1002/anie.198308161

67. Stephen Stoker H *Organic and biological chemistry*, 371. Boston, USA: Cengage Learning. ISBN 978-1-305-68645-8.

68. Delom F, Mallet B, Carayon P, Lejeune PJ. Role of extracellular molecular chaperones in the folding of oxidized proteins. Refolding of colloidal thyroglobulin by protein disulfide isomerase and immunoglobulin heavy chain-binding protein. *J Biol Chem Journal — United States* (2001) 276(24):21337–42. ISSN 0021-9258. doi:10.1074/jbc.M101086200

69. Ushenko V, Sdobnov A, Syvokorovskaya A, Alexander D, Vanchulyak O, Meglinski I, et al. 3D mueller-matrix diffusive tomography of polycrystalline blood films for cancer diagnosis. *Cancer Diagn Photon* (2018) 5(4):54. doi:10.3390/photonics5040054

70. Marchesini R, Bertoni A, Andreola S, Melloni E, Sichirollo AE. Extinction and absorption coefficients and scattering phase functions of human tissues *in vitro*. *Appl Opt* (1989) 28(12):2318–24. doi:10.1364/ao.28.002318

71. Edwards DK, Gier JT, Nelson KE, Roddick RD. Integrating sphere for imperfectly diffuse samples. *J Opt Soc Am* (1961) 51:1279–88. doi:10.1364/josa.51.001279

72. Yildirim Simsir I, Cetinkalp S, Kabalak T. Review of factors contributing to nodular goiter and thyroid carcinoma. *Med Princ Pract* (2020) 29(1):1–5. doi:10.1159/000503575

73. Knobel M. Etiopathology, clinical features, and treatment of diffuse and multinodular nontoxic goiters. *J Endocrinol Invest* (2016) 39(4):357–73. doi:10.1007/s40618-015-0391-7

74. Mallya M, Ogilvy-Stuart AL. Thyrotropic hormones. *Best Pract Res Clin Endocrinol Metab* (2018) 32(1):17–25. doi:10.1016/j.beem.2017.10.006

75. Delitala AP, Capobianco G, Cherchi PL, Dessole S, Delitala G. Thyroid function and thyroid disorders during pregnancy: a review and care pathway. *Arch Gynecol Obstet* (2019) 299(2):327–38. doi:10.1007/s00404-018-5018-8

76. Robinson SP. *Principles of forensic medicine*. Cambridge University Press (1996). 175.